

Study of Micro-porosity in Electron Beam Butt Welding

Debasish Das

Indian Institute of Technology

Soumitra Dinda

Indian Institute of Technology Kharagpur

Amit Kumar Das

Indian Institute of Technology

Dilip Kumar Pratihar (✉ dkpra@mech.iitkgp.ernet.in)

Indian Institute of Technology, Kharagpur

Gour G Roy

Indian Institute of Technology Kharagpur

Research Article

Keywords: Electron beam welding, Micro-porosity, X-ray tomography, Raman spectroscopy, Machine learning algorithms, Monte Carlo Reliability analysis

Posted Date: June 18th, 2021

DOI: <https://doi.org/10.21203/rs.3.rs-533938/v1>

License:  This work is licensed under a Creative Commons Attribution 4.0 International License.

[Read Full License](#)

Study of micro-porosity in electron beam butt welding

Debasish Das¹, Soumitra Kumar Dinda², Amit Kumar Das¹, Dilip Kumar Pratihar*¹, Gour Gopal Roy²

¹Department of Mechanical Engineering, Indian Institute of Technology Kharagpur

²Department of Metallurgical and Materials Engineering, Indian Institute of Technology Kharagpur, India

Email: dd4311@gmail.com; soumitra.dinda@gmail.com; amit.besus@gmail.com;

*dkpra@mech.iitkgp.ac.in; ggroy@metal.iitkgp.ac.in

Phone Number +91 3222 282992, Fax +91 3222 282278

*Corresponding author

Abstract

As complete elimination of porosity from the weld is very difficult, the next option available is to minimize this weld porosity, which is crucial for the safe performance of the welded components. However, this investigation through experiments alone is very tedious and time consuming. Additionally, very limited models are available in the literature for accurate prediction of different porosity attributes. The present study, thus, addressees both the experimental as well as modelling aspect on the study of micro-porosity during *Electron Beam Welding (EBW)* of SS304 plates. Welding parameters are reported to have significant influence on the micro-porosity. Hence, the influences of these parameters on micro-porosity attributes, namely pores number, average diameter, and sphericity are extensively studied experimentally employing optical microscopy (*OM*), scanning electron microscopy (*SEM*), X-ray computed tomography (*XCT*), and Raman spectroscopy. This is followed by an elaborate modelling through seven popular and well-recognized *Machine Learning Algorithms (MLAs)* namely, *Multi-Layer Perceptron (MLP)*, *Support Vector Regression (SVR)*, *M5P model trees regression*, *Reduced Error Pruning Tree (REPTree)*, *Random Forest (RF)*, *Instance-based k-nearest neighbor algorithm (IBk)* and *Locally Weighted Learning (LWL)*. These different techniques enhance the chance of obtaining the better predictions of the said micro-porosity attributes by overcoming the effect of data-dependence and other limitations of individual *MLAs*. The different model-predicted micro-porosity data are also validated through experimental data. Statistical tests and Monte-Carlo reliability analysis are additionally utilized to evaluate the performances of the employed algorithms. *IBk* and *MLP* are overall found to perform well.

Keywords: Electron beam welding; Micro-porosity; X-ray tomography; Raman spectroscopy; Machine learning algorithms; Monte Carlo Reliability analysis.

List of Symbols

A_{ar}	Pore surface area
D_p	Average pore diameter
E	Heat input per unit length
I	Beam Current
L	Total number of welding conditions
N_p	Number of pores
$N_{success}$	Number of successful conditions
N_{total}	Total number of conditions
$O_{ok'l}$	Predicted outputs
$\bar{O}_{ok'l}$	Mean of outputs
$P_{occurrence}$	Probability of success
R^2	Correlation Coefficient
S_{phry}	Average pore sphericity
$T_{ok'l}$	Target outputs
U	Welding Speed
V	Accelerating Voltage
V_{ol}	Pore volume
$AAPD$	Average Absolute Percent Deviation
ANN	Artificial Neural Network
CV	Cross-validation
EBW	Electron Beam Welding
$GTAW$	Gas Tungsten Arc Welding
IBk	Instance-based k-nearest neighbor algorithm
$k\text{-}NN$	k -nearest neighbor
LBW	Laser Beam Welding
LWL	Locally Weighted Learning
$M5P$	Model Trees Regression following M5 algorithm
$MLAs$	Machine Learning Algorithms
MLP	Multi-Layer Perceptron
NDT	Non-Destructive Testing
OM	Optical Microscopy
$REPTree$	Reduced Error Pruning Tree
RF	Random Forest
$RMSE$	Root Mean Square Error
SEM	Scanning Electron Microscopy
SVR	Support Vector Regression
XCT	X-ray Computed Tomography

1. Introduction

The welding process is widely reported to be a complex non-linear system due to various thermo-mechanical-physical-metallurgical phenomena, such as heat transfer, fluid motion, micro-segregation, porosity formation, stress generation, solidification cracking, etc., occurring simultaneously [1, 2]. The welded joint, thus, often acts as a potential site of failure [2]. In particular, *Electron Beam Welding (EBW)* process is often subjected to a higher cooling rate, and the strong influence of *Marangoni, Lorentz*, and *buoyant forces* [3–5]. Thus, under such complex circumstances, weld defect estimation becomes important for quality assurance. Out of the various methods available for the analysis of different welding defects, *Non-Destructive Testing (NDT)* methods have gained wide popularity. Vilar et al. [6] stated that *NDT* methods have been accepted over time from a mere laboratory curiosity to unavoidable need of industrial quality product assurance. As a result, different *NDT* tests have been employed to ensure the quality, longevity, safety, and reliability of products, available in the market [7]. Porosity is one of the prominent welding defects, known to strongly influence the mechanical properties of the joint [8]. Its elimination is also reported to be very difficult [9]. It is seen that porosity promotes the crack initiation, which further reduces the weld fatigue strength [9]. Porosity formation is also reported to be influenced by many factors, namely keyhole dynamics [8, 9], fluid flow, solidification rate [9, 10] etc., but it is observed that weld porosity could be minimized by selecting an optimum set of input process parameters [8, 9].

EBW is known to take place in vacuum environment and the gases responsible for porosity mostly come from the gases inherently dissolved in the base metal. Except the vacuum environment, all the welding processes including *EBW* undergo localized heating, melting, cooling and solidification, which significantly affect the porosity distribution in the weld. Specifically, the cooling rate, keyhole geometry profile, Dendritic Arm Spacing (DAS) etc. of *EBW* and Laser Beam Welding (*LBW*) are comparable, both being high energy welding techniques. Additionally, literature available on the analysis of weld porosity exclusively on *EBW* is relatively less [11]. Hence, regardless of the welding techniques, there are some similarities or trends expected regarding the influence of welding parameters on the porosity distribution in the weld zone. As a result, many different welding techniques are discussed below to address the primary goal of the present study of correlating weld porosity as a function of welding parameters.

Different experimental techniques are utilized by many researchers to study weld porosity.

Sun et al. [9] have investigated the effects of different shielding gases on weld porosity during *LBW* of thick AISI 304 Stainless Steel (SS) plates using a high-speed camera. They have observed a reduction in the porosity size with an increase in welding speed. *LBW* has been carried out by Elmer et al. [12] on A36 steel, 21-6-9 SS, and pure nickel to evaluate the influences of argon (Ar) and nitrogen (N_2) on porosity formation. Both the number of pores and the total pore volumes have been observed to increase simultaneously with the increase in melt volume for AISI 304L SS material-Ar gas combination. Lisiecki [13] has investigated the influence of heat input per unit length (E) on weld-geometry and porosity during *LBW* of 5.0 mm thick S700MC steel plates using Disk laser, where weld porosity has been observed to increase with an increase in the heat input. Wang et al. [10] have conducted *LBW* of 2 mm thick 5754 Al-alloy sheets to investigate the effects of welding process parameters on the joint quality. They have also carried out X-ray inspections to study the weld porosity and have found it to decrease with the reduction of heat input. Blecher et al. [14] have studied root defects in fully penetrated laser and hybrid laser arc welding using optical microscopy (*OM*) and X-Ray CT scan. They have observed root defect formation to strongly depend on a force balance between the surface tension and melt-pool weight. This force balance has been observed to depend strongly on heat input and could be minimized by preferring low heat input. *EBW* of mild steel and Fe-Al alloy has been carried out by Dinda et al. [11], where an increase in weld porosity has been observed with an increase in welding speed. Moreover, they have suggested the use of beam oscillation to reduce porosity formation. *XCT* and Raman spectroscopy has been performed by Bandi et al. [15] to investigate micro-porosity during *EBW* of Zircaloy-4 alloys. They have also reported a significant reduction in porosity by using an oscillating beam. X-ray Diffraction (*XRD*), *SEM*, *XCT*, and micro-hardness tester have been used by Dinda et al. [16] to study the distribution of porosity and intermetallic compounds (*IMCs*) in dissimilar *EBW* of DP600-steel to 5754 Al-alloy. They have also observed a significant reduction in the porosity due to beam oscillation. They have further employed Raman spectroscopy for gas identification in the welds. The amplitude of oscillation is also observed to have a strong influence on the pore attributes through the *XCT* [17]. Alshaer et al. [18] have studied the weld defects and mechanical performance of LB-welded AC-170PX Al-alloy using fillet and flange couch joints. They have reported an increase in porosity with an increase in welding speed and heat input. *OM*, *SEM*, etc. have been utilized by Zhan et al. [19] to study the influence of heat input on porosity during laser cladding of Invar alloy. They have reported heat input and cooling rate to have the

significant influence on the porosity, where the porosity has been observed to increase as a function of heat input until a threshold value, after which it is also observed to follow the decreasing trend. Xie et al. [20] have carried out *XCT* and *SEM* to investigate the influence of heat input on porosity during the *LBW* of Molybdenum alloy and have observed an increase in porosity with an increase in the heat input. They further have reported that porosity occurs at low heat input due to the inability of the gases to escape the weld zone because of the high cooling rate.

Apart from experimental investigation, the capability of different conventional and non-conventional modeling techniques have been widely explored by various researchers to predict the desired weld attributes [3]. Among many such available techniques, Statistical Regression Analysis (*SRA*) is reported extensively for modeling various *EBW* processes [21] using experimental data set. However, it is known that human error, machine error, process error etc. always contribute to some uncertainties in any experimental data set. These uncertainties are rightly expected to be present in the augmented data set, obtained through the regression equations. On the other hand, the use of *Machine Learning Algorithms (MLAs)* generally requires a large data set for satisfactory performances and is usually observed to yield unsatisfactory results with the smaller data set [1]. At the same time, *MLAs* can handle the uncertainties and complexity of the problem in an efficient way, it is also reported to offer a noticeable improvement in the quality of prediction [1]. Thus, the outstanding state-of-the-art performances, accurate predictions and better generalization capability of the *MLAs* using an augmented data set offer a popular choice for the modeling of different processes [1]. The influence of input parameters, namely power, welding speed, stand-off distance and clamping pressure on the quality of *LBW* has been investigated by Petkovi [22]. The researcher has employed *SVR*, *ANN* etc., where the *SVR* has performed better than others. Liang et al. [23] have stated that *SVR* performs better than *MLP* for the same small size dataset during the prediction of weld attribute in gas tungsten arc welding (*GTAW*) of AISI 304SS. Boersch et al. [24] have used *M5P*, *RF*, *SVM* and a few other *MLAs* with the help of Weka software to predict the weld diameter during resistance spot welding. The deviation in the model-predicted weld diameter found to be within 10% with respect to the experimentally measured one for most of the datasets. Computational intelligence-based tools, such as *MLP* and radial basis function networks have been used by Ghanty et al. [25] to investigate the influences of different welding parameters on the melt-pool geometry during *GTAW* of AISI 316LN stainless steel material. These *SRA* and other *MLAs*-based modeling techniques have also been utilized to predict

the influence of welding process parameters on porosity and other welding defects. A 3D transient model has been proposed by Lu et al. [8] to study the effects of process parameters on keyhole-induced porosity during the *LBW* of CCS-B steel, where the predictions closely matched the experimental results. They have observed pore number and its size to increase with an increase in laser power and a decrease in welding speed. On the other hand, Munir et al. [26] and Hou et al. [7] have employed various *MLAs* to study welding defects, namely cracks, porosity, slag inclusion etc. *MLP* and fuzzy k-nearest neighbor are employed by Wang and Liao [27] to identify different welding defects from the radiographic images. They have found *MLP* neural networks to perform better than fuzzy- k-nearest neighbor (*k-NN*). Liao et al. [28] have used *MLP* and case-based reasoning (*CBR*) to predict welding defects. Das et al. [29] have summarized the merits, issues and guidelines for the selection of the most suited conventional and non-conventional techniques for efficient weld optimization.

As mentioned above, complete elimination of porosity from the weld is very difficult. Hence, the second-best option available is to minimize this weld porosity, which is crucial for the safe performance of the welded components. However, the experiment-based detection of porosity in weld, followed by its proper analysis is very time consuming and tedious. As a result, generation of a large data-set on weld porosity through experiments alone is infeasible within a given time. This also make modelling and optimization of weld porosity, slag inclusion, crack or any other welding defects extremely difficult [1, 7]. These above stated issues have led to limited availability of literature on the experimental, modelling and combined analysis of weld porosity in *EBW* [11].

The novelty of the present study, thus, lies with the detailed experimental investigation of the effects of welding input process parameters on the above stated gas-induced micro-porosity attributes during the *EBW* process through *OM*, *SEM*, *XCT*, and Raman Spectroscopy. The study also evaluates the role of the melt-pool area on the gas escape. In addition, seven popular and well-recognized *MLAs*-based models from distinctly different backgrounds are chosen for the present study, that is, *Multi-Layer Perceptron (MLP)* and *Support Vector Regression (SVR)* works on the principle of artificial neural network (*ANN*). *M5P* model trees regression, *Reduced Error Pruning Tree (REPTree)* and *Random Forest (RF)* are tree-based regression tools. *Instance-based k-nearest neighbor algorithm (IBk)* and *Locally Weighted Learning (LWL)* belong to lazy learning-based algorithms [30, 31]. Hence, *MLAs* corresponding to different categories, namely neural networks, model regression trees and lazy-learner are likely to overcome this data-dependence of the *MLAs*,

compensate the limitations of individual algorithms, and thereby, significantly improve the chance of obtaining the better results. Moreover, a well-known K -fold cross validation (CV) technique is adopted in the present study using the employed *MLAs* to make the modelling rigorous, thorough and unbiased [30, 32–34]. Additionally, these models are also validated through experiments. Some well-known statistical tests along with Monte-Carlo reliability analysis techniques are also utilized to evaluate and thereby, compare the capability of the *MLAs* to predict micro-pore attributes in the weld.

Hence, the present study brings together an extended experimental investigation, a wide variety of popular *MLA*-based modelling techniques and their performance evaluation through statistical tests and Monte-Carlo reliability estimation to analyze micro-porosity formation as a function of the high energy-based *EBW* input parameters under one roof. Such a balanced and elaborate study on similar topic is very limited. Hence, the present study has added value to the research community and thereby, assist in the selection of suitable process parameters in order to reduce the weld porosity.

It is necessary to mention that other than welding process parameters optimization, the use of beam oscillation has also been reported to effectively reduce weld porosity. However, it also consists of different parameters, namely beam oscillation frequency, beam oscillation radius and various modes of beam oscillation, such as circular, triangular, rectangular etc. [16, 35, 36]. As stated above, experimental investigation of the influence of these different beam oscillation parameters on weld porosity is time taking. Moreover, in order to develop input-output models, a large experimental data will be beneficial following full-factorial design, Taguchi or any other Design of experiments (*DOE*). As a result, this also requires a separate in-depth investigation, for which it is kept for future studies. The authors also plan to combine the optimum beam oscillation parameters with the optimum welding input process parameters, in future, which is expected to further reduce weld porosity and thereby, further improve the joint quality.

The rest of the manuscript is structured as follows: Section 2 deals with a brief description of the employed materials and methods for the experiment. Section 3 discusses the different *MLAs* used in this study. Results are stated and discussed in Section 4. Some concluding remarks are made in Section 5.

2. Experimental Study and Data Collection

The experimental setup and methods of data collection and data augmentation used in the present study are briefly discussed, in this section.

2.1. Experimentation

It is to be noted that the welding samples are cleaned with acetone to remove all the dirt particles prior to carrying out the welding. Experiments are conducted on an 80kV-150mA *EBW* set-up, developed by Bhabha Atomic Research Centre, Mumbai, India [34, 37] at IIT Kharagpur, India (refer to Fig. 1(a)). The working ranges of input process parameters used in the present study are listed in Table 1. The welding parameters used in the present study are selected by considering the working ranges of the process parameters reported in literature [34, 37] and through some prior trial and error welding runs within the working range of the available *EBW* setup. It is important to note that 5 mm thick AISI 304 SS plates are butt welded, and its chemical compositions are found to be 71.37% Fe, 17.80% Cr and 8.09% Ni through X-ray fluorescence spectroscopy (*XRF*) [38]. It is to be noted that AISI 304 stainless steel has been extensively used in the chemical industries, nuclear reactor coolant piping, fabrication plants, food processing industries, dairy industries, cryogenic vessels, valves systems industries, and in numerous other sectors due to its outstanding mechanical properties at the elevated temperatures, strength, corrosion resistance etc. [39, 40]. This makes the present investigation more crucial.

Table 1. Working range of input process parameters used in the present study.

Input Process Parameters	Symbols	Three levels of inputs		
Accelerating voltage (kV)	<i>V</i>	60	65	70
Beam current (mA)	<i>I</i>	80	87	94
Welding speed (mm/min)	<i>U</i>	750	1200	1650

The weld samples corresponding to $3^3 = 27$ different welding conditions (according to full-factorial design of experiments) are polished on a Supertech double disc polishing machine using Jawan brand silicon carbide waterproof paper with the grit sizes of 220, 400, 600, 800, 1000, 1200, followed by diamond polishing at 0.25 μm . Polishing is then followed by etching using a

mixture of Ferric chloride, Hydrochloric acid, and Ethyl alcohol in the approximate ratio of 20%, 5%, and 75%, respectively. The obtained weld cross-section is then investigated through *OM* and *SEM*. The *OM* is carried out on Leica DMLM optical image analyzer at Optical Microscopy and Material Testing (*OMMT*) Laboratory, Central Research Facility (*CRF*), IIT Kharagpur, India. Similarly, *SEM* images are taken from JEOL JSM-IT300HR, Department of Metallurgy and Materials Engineering, IIT Kharagpur, India, for observing the better and magnified views of pores. The successful identification of the pores has led the authors to carry out extensive *XCT* analysis of all the 81 welded samples (corresponding to all $3^3 = 27$ different welding conditions according to the full-factorial design of experiments (*DOE*)) through the Zeiss versa 520 system (refer to Fig. 1 (b)). It is to be noted that the non-destructive *XCT* analysis is used for 3D visualization and quantification of micro-porosity in the weld. It is important to note that the samples are not etched before carrying out the *XCT* analysis, as it may enlarge the porosity. The sample is mounted on a table lying between the X-ray gun and the detector screen. The table is rotated 360° and several images are taken throughout the rotation. All these images are merged to develop the 3D volumetric image of the sample, also known as 3D pixel or simply voxels. The machine is further equipped with different optical systems to obtain additional magnification. The *XCT* data are analyzed through VG-STUDIO-MAX 2.2 software. The noise present in the 3D images, because of the unexpected tilt or shift of the sample during testing due to fixation issues, is addressed through the proper smoothening processes. ROI CT filtering and beam hardening correction (BHC) are performed to eliminate the ring effects and artifacts, respectively, by maintaining the histogram between the matrix and background. A thresholding value of 0.1 is maintained for all the analyses [11, 16, 41]. The *XCT* machine parameters, namely voltage, current, exposure time, filter (Cu-mm), number of projections, and voxel size are kept equal to 150 kV, 150 μ A, 500 mS, 0.5 (Cu-mm), 1000, and 23.8 μ m, respectively. The micro-porosity in the weld is measured in the present study following (ISO15901, part 3; 2006 (EN)) standards. During *XCT* analysis, it is ideally desirable to scan the entire weld sample to study the pore distribution through *XCT*. However, in practice, it may not always be feasible. That is, the X-Rays need to penetrate the full-size sample completely in order to map the variation in density of the metal and gases. As the X-Rays fail to penetrate the full-size sample even with the above stated maximum rated voltage and current settings with intermediate number of projections of the *XCT* machine, a reduction of the sample size becomes a compulsion. To maintain consistency, the size of all the porosity

samples used for the said *XCT* analysis are kept same and these samples are cut from approximately the same location of the welded plate. That is, from the welded plate of size 110 mm × 80 mm × 5 mm, a small portion of the plate of size 15 mm × 15 mm × 5 mm is cut at the center of the plate, which is located at a distance of 40 mm from the starting point of welding start point and 40 mm from the end of the weld, and it is shown in Fig. 1 (c). As the sample size is reduced, the X-Rays can now fully penetrate the sample, and the possibility of detecting smaller pores through *XCT* also increases. For the said sample size (15 mm × 15 mm × 5 mm), the voxel size is found to be equal to 23.8 μm. However, a minimum resolution of one micron is kept just to indicate that even smaller pores may be available, whose measurement is beyond the scope the present study. Thus, in order to detect even the smaller pores, the sample size needed to be reduced further. But, that again would limit the analysis of pore distribution in a very small weld zone. The authors carried out a few trial-and-error runs to decide the size of the samples. After completing the *XCT* analysis, the entrapped gasses in the *EBW* samples are then determined through Raman spectroscopy [11, 42–44] (refer to Fig. 1(d)). Fig. 1 shows all the experimental setup used in the present study. It also shows the complete welded sample, the place from which samples for porosity analysis are taken, and the sample used for porosity analysis of the welding conditions. Raman spectroscopy, employed in the present study for gas detection uses Argon-Krypton mixed ion gas laser. MODEL 2018 RM (Make Spectra-Physics, USA) and MODEL T64000 (Make Jobin Yvon Horiba, France) are used as the excitation source and spectrometer, respectively. The thermo-electric cooled front-illuminated 1024 256 CCD of MODEL SynpseTM (Make Jobin Yvon Horiba, France) and Optical Microscope of MODEL BX41 (Make Olympus, Japan) are used as the detector and collection optics, respectively. The focal length, frequency, step size, and grating during the Raman spectroscopy are kept equal to 640 mm, 100 cm⁻¹, 0.00066 nm, and 1800 grooves/mm, respectively [11, 41, 43, 44]. Finally, the melt areas corresponding to the said welding conditions are obtained from the weld cross-section through microscopy study. All the experimental and modelling steps adopted in the present study are graphically presented through a flowchart (refer to Fig. 2). This representation not only provides a compact summary of the entire work but also guides the young researchers how to proceed stepwise.

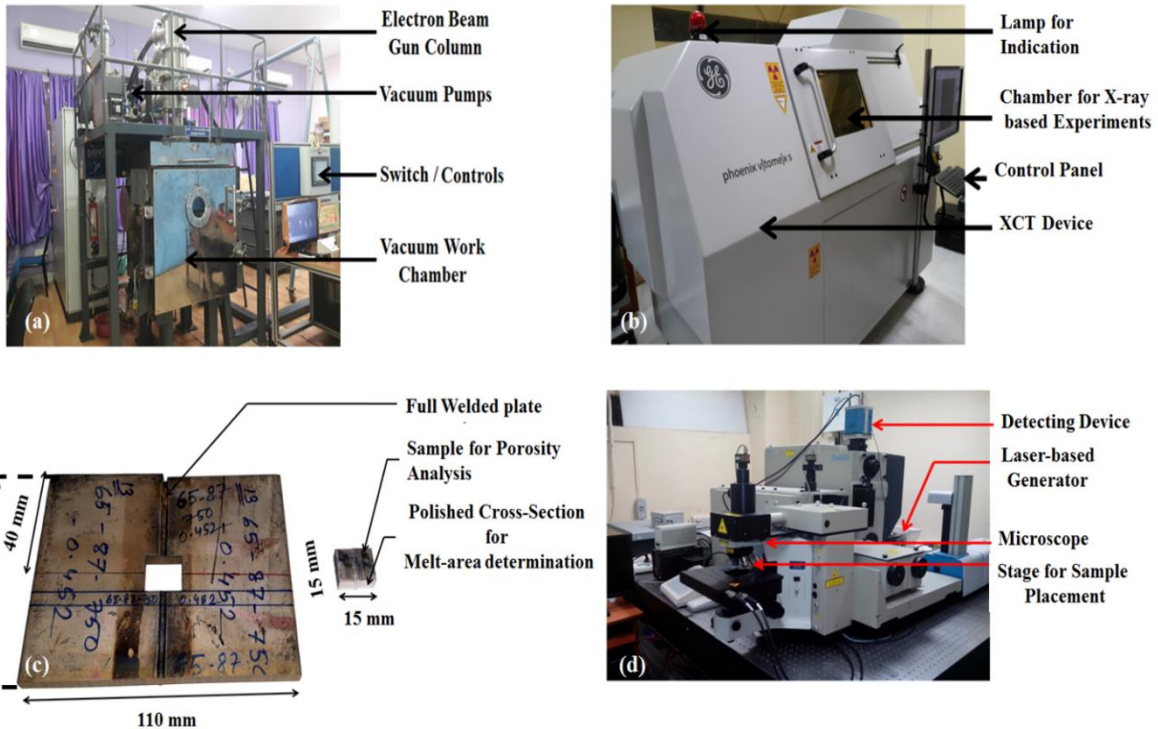


Fig. 1. Photograph of a) EBW Set-up, b) XCT Set-up, c) welded joints with XCT specimen's dimensions, and d) Raman spectroscopy Set-up.

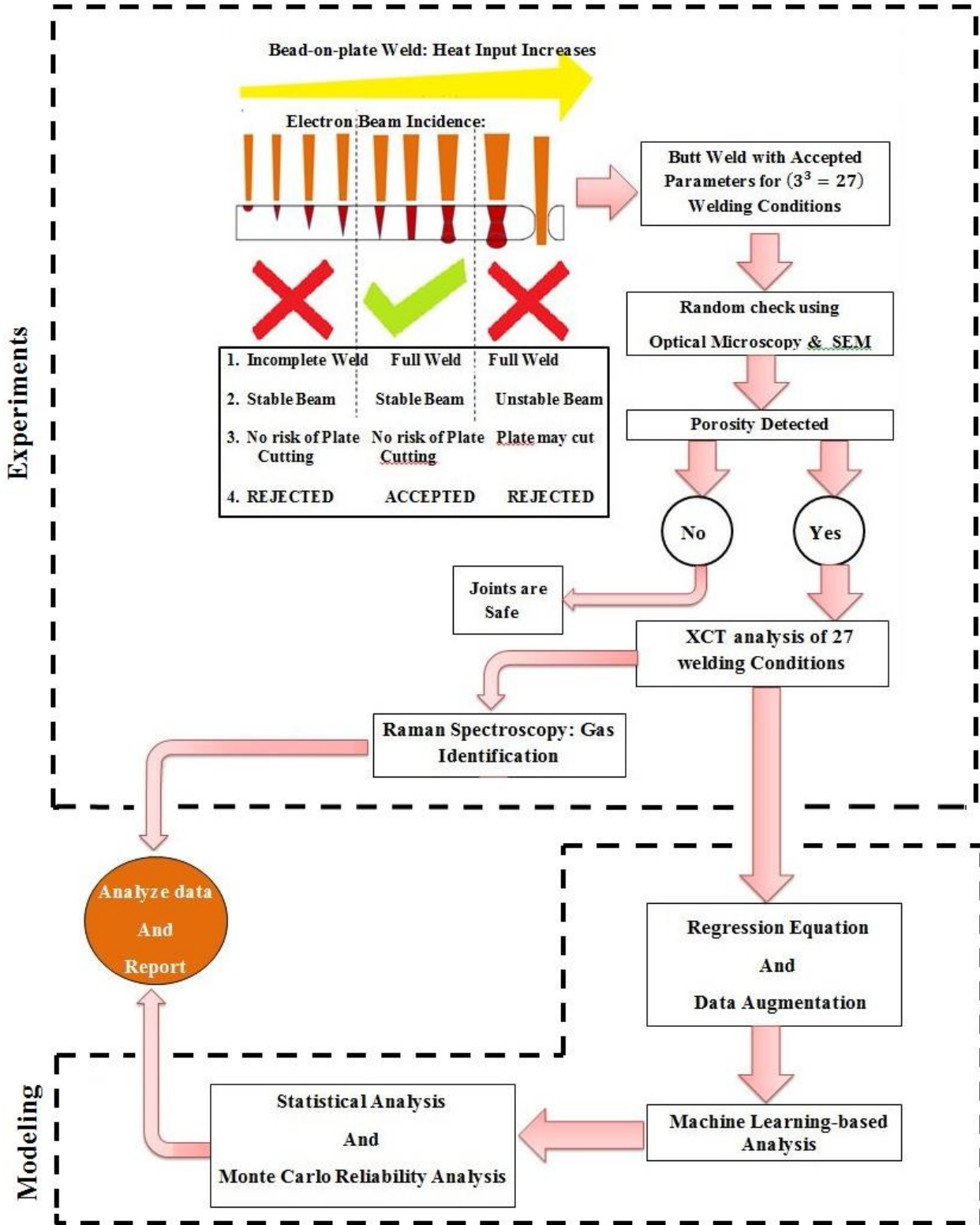


Fig. 2. Flowchart depicting the stepwise detection, modeling and analysis of micro-porosity in weld.

In this study, V , I , and U are considered as input parameters (refer to Table 1). The number of pores (N_p), average pore diameter (D_p) (μm) and average pore sphericity (S_{phry}), are considered as the outputs. Here, full-factorial design with the said three input parameters having three levels each is developed. Thus, weld porosity for each of the $3^3 = 27$ possible combinations of input process parameters are experimentally measured. Three sets of welding corresponding to the said 27 different conditions are conducted and their average values are reported to maintain uniformity and consistency of the results. Hence, *XCT* analysis of a total of $27 \times 3 = 81$ samples are conducted. Moreover, the combined influences of V , I and U are frequently represented in the literature in terms of heat input (E) (kJ/mm) (refer to Eq. 1) [45].

$$E = \left(\frac{VI}{U} \right), \quad (1)$$

Here, heat input is varied from 0.175 kJ/mm to 0.526 kJ/mm .

2.2. Data augmentation

As stated above, a large data-set is usually required for satisfactory performance of the *MLAs* [1]. However, generating a large data set on weld porosity, slag inclusion, crack or any other welding defects are time consuming and difficult to obtain, thereby making the use of *MLAs*-based techniques for modelling and prediction very challenging. This issue with small data set is addressed by some researchers with reasonable accuracy by employing different data augmentation techniques to increase the size of the original data set. In fact, they have recommended this approach for the use of numerous *MLA*-based modelling and prediction of different metallurgical outputs with relatively small database [1, 7]. Thus, the idea of data augmentation technique adopted in the current investigation is inspired from the published literature [1, 7] and thus justifies the approach adopted in the present study. In addition, some uncertainties are always associated with the experimental data and these are likely to be also present in the augmented data developed through regression equations. Moreover, *MLAs* can inherently deal with these uncertainties and inconsistencies associated with the augmented data [1]. This is further accompanied by the use of well-known K-fold cross validation (CV) technique, known to make the evaluation of the performance of the *MLAs* unbiased and thorough [30, 32, 33].

Hence, the experimental data available in the present study for only $3^3 = 27$ input-output combinations utilizing a full-factorial data set is artificially augmented to 1000 input-output data set by generating additional 973 input-output data using regression equations (refer to Eq. 2-4) developed through Minitab 16 software. The equations used for the data enhancement are given below.

$$N_p = -5798 + 125V + 89.6I + 8.78U - 1.80VI - 0.169VU - 0.122IU + 0.0023VIU \quad (2)$$

$$D_p = 33 + 0.2V + 0.17I + 0.117U + 0.005VI - 0.00226VU - 0.00165IU + 0.000024VIU \quad (3)$$

$$S_{phry} = 0.723 - 0.00154V + 0.000222I + 0.000084U \quad (4)$$

The quality of the *MLAs*-based predictions are evaluated through $R^2 \left(1 - \frac{\sum_{l=1}^L (T_{ok'l} - O_{ok'l})^2}{\sum_{l=1}^L (T_{ok'l} - \bar{O}_{ok'l})^2} \right)$, $RMSE \left(\sqrt{\frac{\sum_{l=1}^L (T_{ok'l} - O_{ok'l})^2}{L}} \right)$ and $AAPD \left(\frac{1}{L} \sum_{l=1}^L \left| \frac{T_{ok'l} - O_{ok'l}}{T_{ok'l}} \times 100 \right| \right)$ [34], where $R^2, RMSE, AAPD, L, T_{ok'l}$ and $O_{ok'l}$ denote the correlation coefficient, root mean square error, average absolute percent deviation, total number of welding conditions, target and predicted outputs of l^{th} condition, respectively.

3. Tools and techniques for modeling through *MLAs*

WEKA (Waikato Environment for Knowledge Analysis) is a well-accepted open-source java-based machine-learning framework consisting of a diverse categories of *MLAs* for regression, classification and other data processing [34, 46–48]. The present study utilized Weka 3.8.0 to develop *MLP*, *IBk*, *RF*, *REPTree*, *SVR*, *M5P* and *LWL*. *MLP* is an artificial neural network (*ANN*) comprising of the input, hidden and output layers architecture [30]. It works based on the principle of back-propagation. It has also been employed by many other researchers [27]. *IBk* is an instance-based lazy learner regression tool, and works based on the *k-nearest neighbor (k-NN) algorithm*. The Euclidian distance of the instances are utilized to denote the nearest neighbors [30, 49]. *RF* is an efficient tree-based *MLA* capable of carrying out both classification

and regression [50]. *RF* has also been reported by various researchers for the prediction of different weld attributes [51, 52], and found to be very accurate. However, very limited applications are available in the field of high energy welding and joining processes [47]. Node statistics-based multiple decision tree, used for regression and classifications is called *Reduced Error Pruning Tree* ("REPT") [30, 53]. Vapnik et al. [54] have developed a statistical approach-based supervised *MLA*, known as Support vector machine (*SVM*). It has gained popularity and implementation in welding industry because of being less time-and cost-taking technique for modeling of data than that of *ANN* models [55]. It employs a kernel function to solve the problem [23]. *Model Trees Regression* (*M5P*) uses the M5 algorithm and works based on the principle of divide-and-conquer policy. It is relatively smaller than other trees and also contains a fewer variables [30]. Zhan et al. [56] reported that *M5P* algorithm could create multiple linear regression models at its tree leaves. Alam et al. [50] stated that *M5P* regression tree is generated through piecewise function of many linear models. *LWL* is a non-parametric statistical tool, which depicts the non-linearity of a problem through piece-wise linear simplification [30, 57]. Here, Weka 3.8.0 is used to develop *MLP*, *IBk*, *RF*, *REPTree*, *SVR*, *M5P* and *LWL*.

4. Results and discussion

Various observations, made by the authors are discussed below. It consists of the detection of the micro-pores in weld through *SEM* and *XCT*, followed by the study on change in micro-pore attributes with heat input and the identification of gases through Raman Spectroscopy. This is followed by data augmentation using regression equations and *MLA*-based modeling. Finally, the performances of these modeling techniques are evaluated through statistical tests and Monte Carlo Reliability Estimation.

4.1. Micro-pore detection through *SEM* and *XCT*

Micro-pores in the weld cross-section are detected through *SEM* study, as shown in Fig. 3 (a) and 3 (b), respectively, for both the etched and un-etched samples. It is to be noted that the authors have used both the etched and un-etched *SEM* images of the weld cross-section to identify and thereby, confirm the presence of pores in the weld samples. This is so, because the pores are relatively easier to identify in the etched samples. However, there is a possibility that the spot identified as a pore may have been formed due to pitting, which leads to an error in identification. This possibility of obtaining error is nullified by successful pore identification in the un-etched polished samples. However, the visibility or the ease with which it could be identified is relatively

less. Thus, the images of both the etched and un-etched regions are provided in the present study to confirm the presence of distinctly clear micro-pores in the weld. The confirmed pore identification has led the authors to conduct an extensive investigation of the effects of welding process parameters on pore attributes through *XCT* analysis. It provides a detailed 3D distribution of micro-pores in the weld samples.

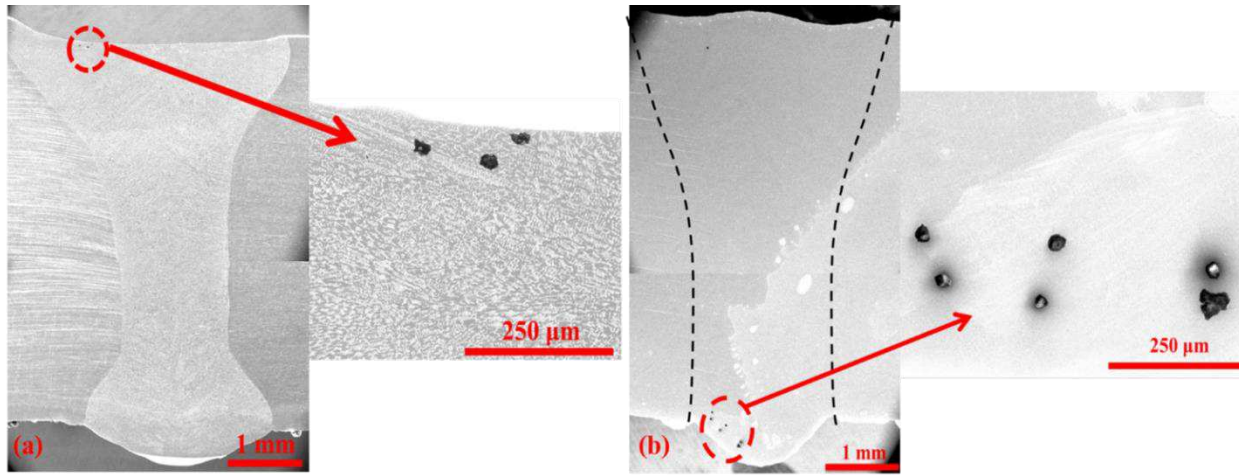


Fig. 3. SEM images showing porosity of both (a) etched, (b) unetched polished welded samples.

XCT study works based on the density difference occurred between the porosity and the matrix. The volume percentage of porosity is calculated with respect to the total scanned volume [14]. Fig. 4 depicts *XCT* results of pores distribution in the weld plate, where the micro-pores of different sizes are observed to be distributed throughout the weld fusion zone. It is to be noted that the variation of porosity from the weld centerline to the further extent of the weld zone on both the sides is not considered. It is so, because the weld porosity is mainly formed due to the melting and solidification in the fusion zone, and consequently, porosity is observed within the fusion region only but not in the heat affected zone (*HAZ*) or unaffected base metals.

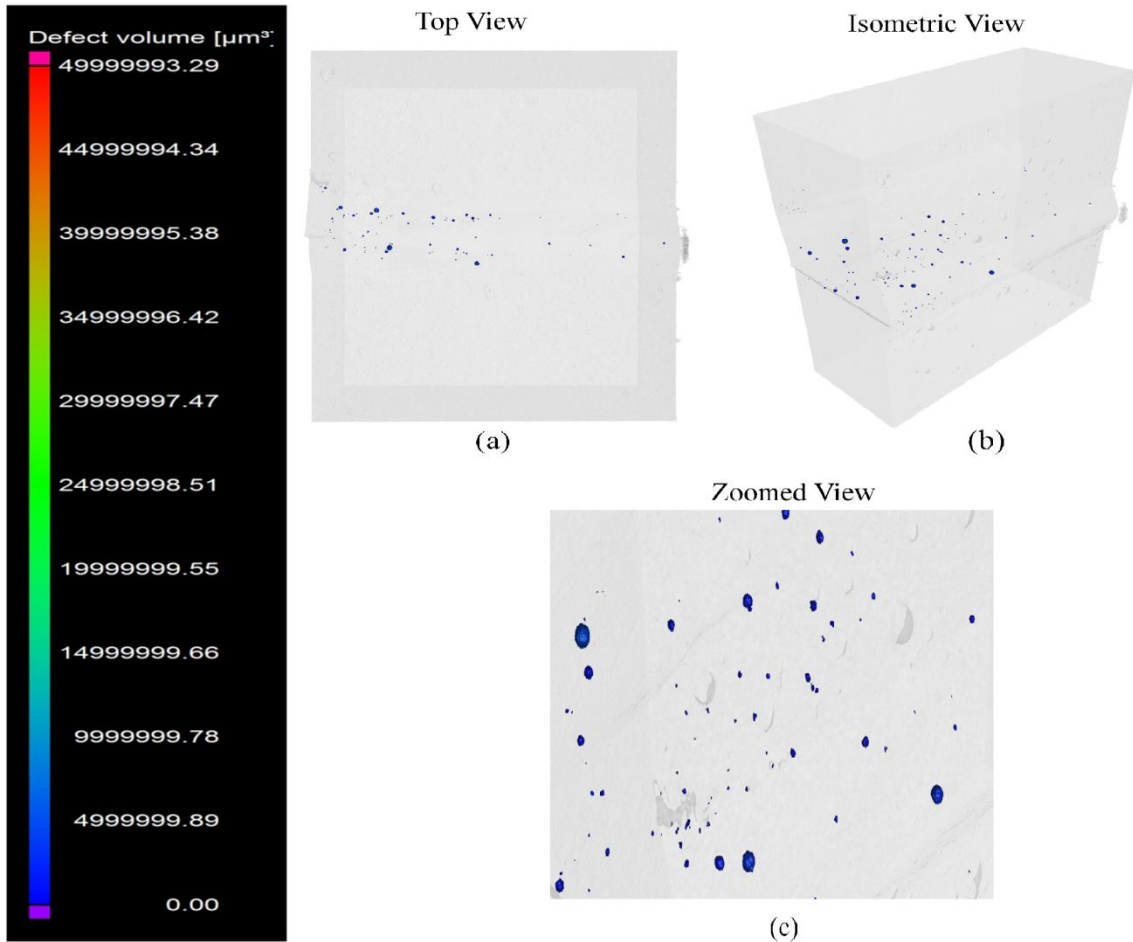


Fig. 4. 3D *XCT* result showing porosity distribution of a joint: a) top view, b) isometric view, c) zoomed view.

4.2. *E* vs. different micro-porosity features

The nature of variation of weld porosity with heat input is shown in Fig. 5. From Fig. 5, it can be observed that as *E* is increased from 0.175 kJ/mm to 0.239 kJ/mm, N_p increases from 3 to 522, and D_p varies from 32 μm to 39.08 μm . The authors further observed that the percentage of porosity has increased from $7.3 \times 10^{-6}\%$ to $2.6 \times 10^{-4}\%$, whereas the average pore volume is increased from $1.08 \times 10^{-5}\text{ mm}^3$ to $2.75 \times 10^{-5}\text{ mm}^3$. This observation is in line with the literature [8–10, 12, 13].

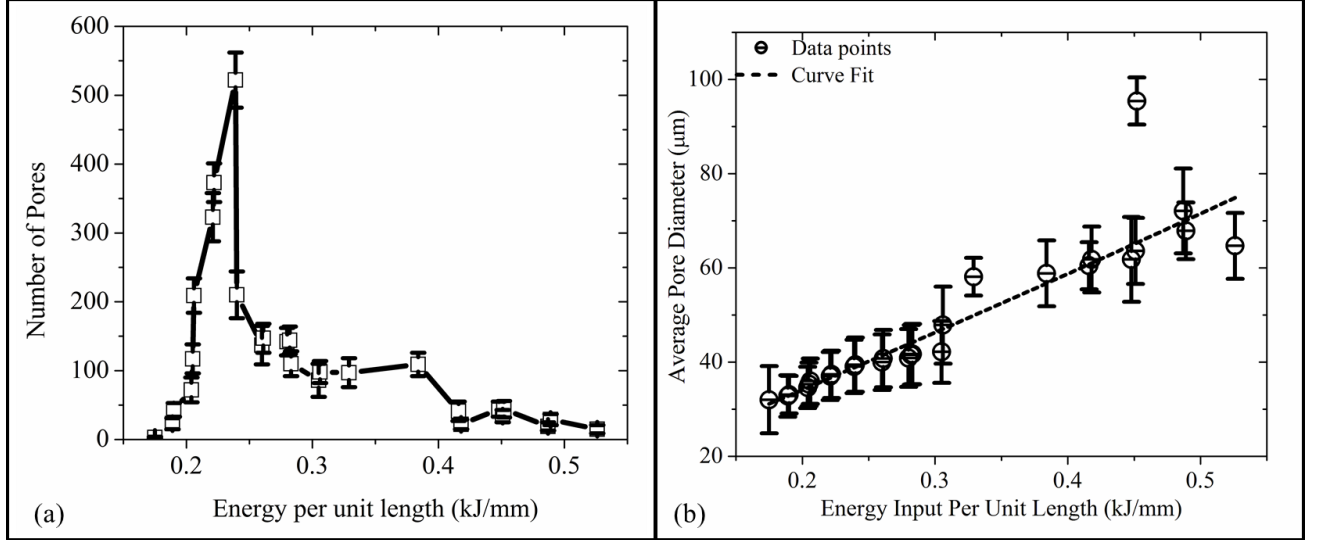


Fig. 5. E vs. a) number of pores (N_p), b) average pore diameter (D_p) (μm).

This is so, because an increase in E leads to an increase in the volume of material melted. This also increases the turbulence and fluid flow, occurring in the melt-pool [13, 58], resulting into an enhancement of porosity in the weld. It is to be noted that E of 0.239 kJ/mm corresponds to the maximum N_p . However, as E is further increased from 0.240 kJ/mm to 0.452 kJ/mm, N_p is observed to gradually decrease from 210 to 44, respectively, but D_p is observed to increase from 39.45 μm to 95.42 μm . The percentage of porosity is also observed to increase from $4.05 \times 10^{-4}\%$ to $5.36 \times 10^{-3}\%$. The average pore volume is also seen to increase from $3.04 \times 10^{-5} \text{ mm}^3$ to $9.65 \times 10^{-4} \text{ mm}^3$. Hence, apart from N_p , all other parameters have followed the expected trends, as reported in the literature [8–10, 12, 13]. N_p is also observed to decrease, even though the pore volume is increased. This is so, because with the increase in E , liquid melt-pool gets more time and energy, which will help to create more porosity eventually, but due to the prolong time and more opening time of melt-pool, coalescence of small pores to form the bigger one is also carried out. Similar observations on the change in porosity attributes as a function of heat input, role of cooling rate on the restriction of gas movement out of the melt zone etc., have been reported in the literature [19, 20, 59]. It is interesting to note that as E is increased further from 0.487 kJ/mm to 0.526 kJ/mm, N_p is decreased from 19 to 15. The porosity percentage is also decreased from $4.65 \times 10^{-3}\%$ to $2.38 \times 10^{-3}\%$. The average pore volume and D_p are also found to decrease from 7.09×10^{-4}

mm^3 to $2.75 \times 10^{-4} \text{ mm}^3$ and $72.09 \mu\text{m}$ to $64.69 \mu\text{m}$, respectively. This might be due to a further increase in the solidification time, for which the bubbles could escape the melt-pool, which leads to a decrease in weld porosity. Similar observations have also been reported in the literature [10]. Moreover, an increase in E has increased in the overall melt area. The pores get a larger area to escape from the melt-pool. As a result, the decrease in the porosity may be attributed to the increase in solidification time and melt area, which allows the pores to escape from the melt zone. The change in the average melt area with E is shown in Fig 6.

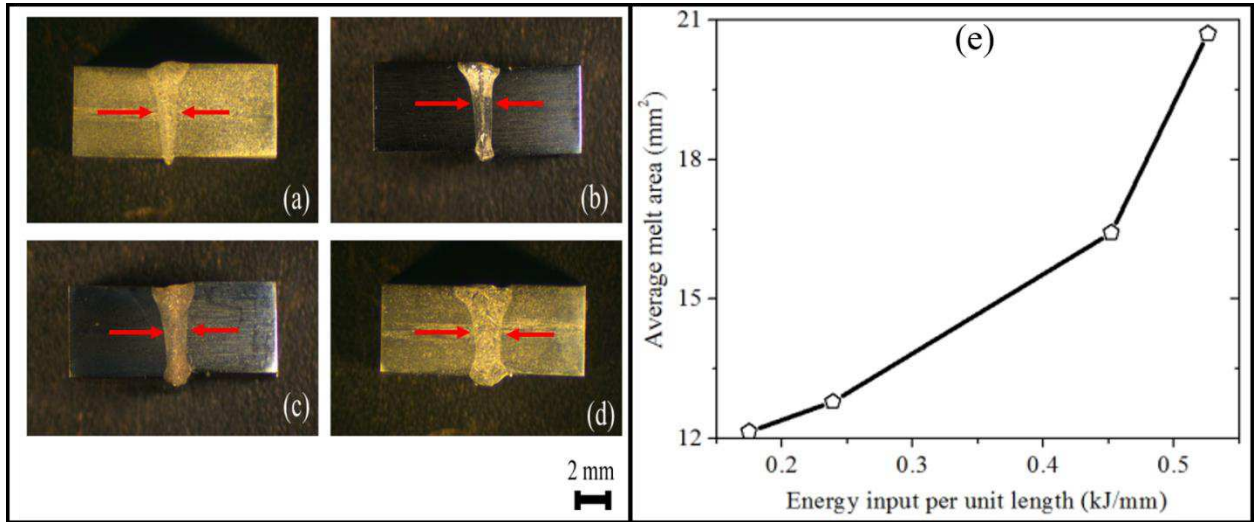
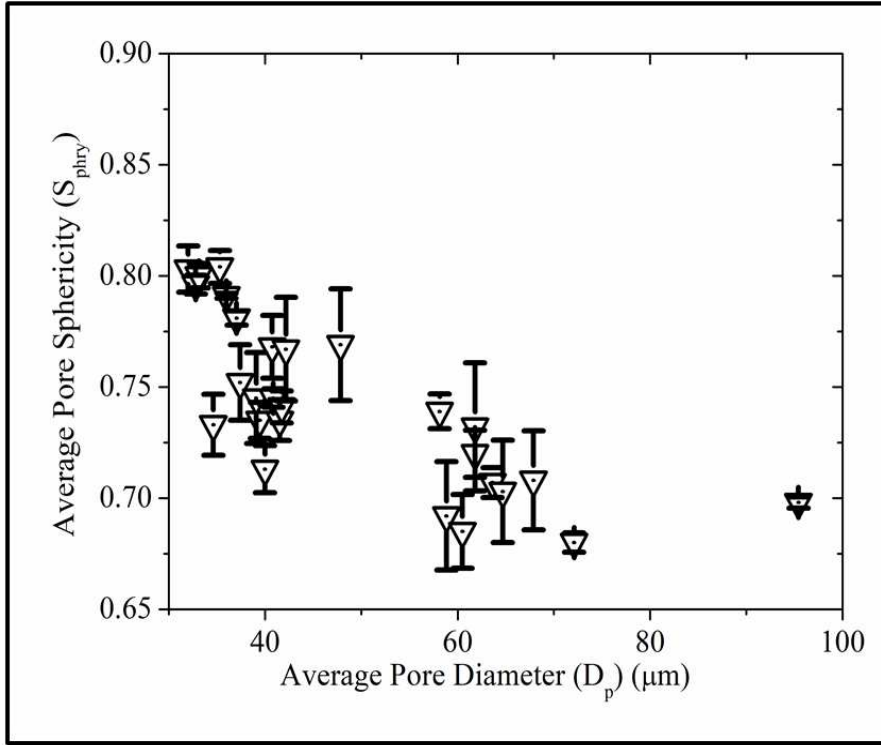


Fig. 6. Melt area (red marked) corresponding to a) 0.175 kJ/mm , b) 0.239 kJ/mm , c) 0.452 kJ/mm , d) 0.526 kJ/mm , e) change in average melt area with E .

Furthermore, S_{phry} is used to define the 3D-shape of the pores. It varies from 0 to 1, which corresponds to a completely non-spherical and perfectly spherical pore, respectively. It is calculated through Eq. (5), where the pore volume and pore surface area are denoted by V_{ol} and A_{ar} , respectively. Moreover, S_{phry} is plotted concerning D_p in Fig. 7. The obtained trend is in line with the literature [11].

$$S_{phry} = \frac{\pi^{1/3}(6V_{ol})^{2/3}}{A_{ar}}, \quad (6)$$



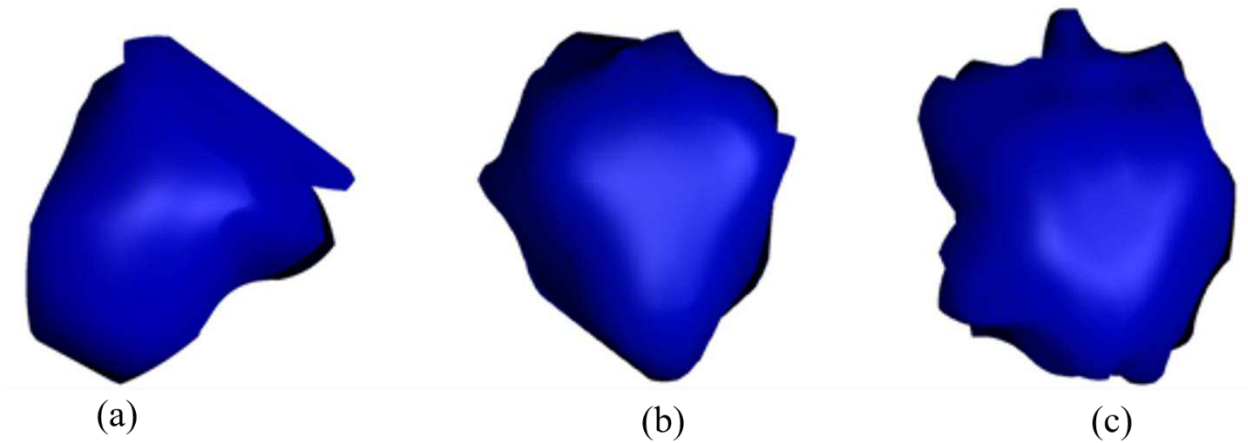


Fig. 8. 3D-reconstructed pore with S_{phry} values of a) 0.68, b) 0.743, c) 0.804.

4.3. Gas detection through Raman spectroscopy

Porosity is mainly induced by the entrapment of different gasses. Gases may be entrapped during the manufacturing of base metal. A few air pockets may also be entrapped within the metal junction during the mechanical assembling, though *EBW* is carried out in a vacuum environment [16, 36, 60]. *EBW* is a very high speed and high cooling rate process, due to which, some gases may be entrapped during welding solidification. Moreover, some gases may also be inherently dissolved into the workpiece itself. Huang et al. [60] have observed a significant contribution of residual hydrogen gasses to the formation of gas-induced porosity in *EBW*. They have further suggested that the entrapped gas-induced porosity has an overall spherical morphology. Williams et al. [61] have observed a strong influence of input process parameters on the pore morphology during additive manufacturing through *XCT* analysis. Results of Raman spectroscopy, conducted in the present study, are provided in Fig. 9. It shows the variation of intensity with the Raman shift. The peaks are observed experimentally at approximately 2332 cm^{-1} and 3020 cm^{-1} Raman shift, which confirms the presence of entrapped nitrogen and hydrogen gases, respectively. The absence of any other peaks in Fig. 9 confirms the presence of no other gases, contributing to the weld porosity formation. This study is found to be in line with the observations reported in the literature [11].

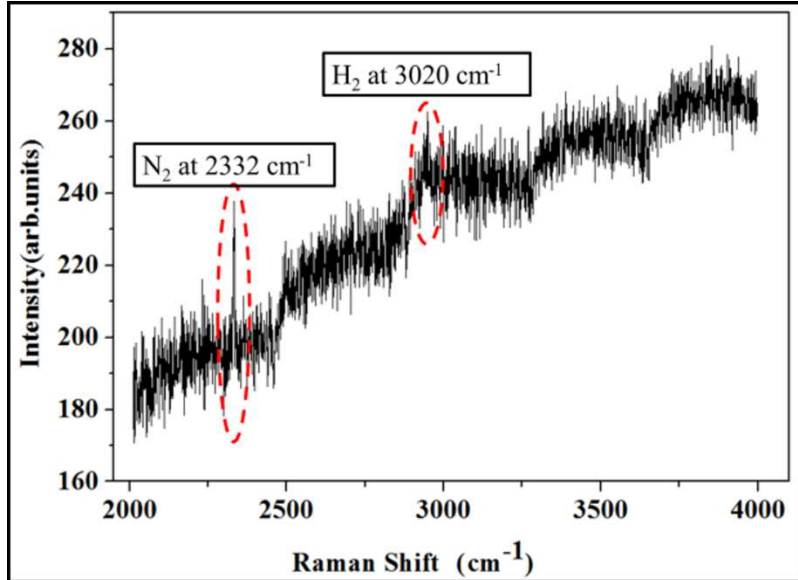


Fig. 9. Detection of hydrogen and nitrogen gases in *EBW* samples through Raman Spectroscopy.

4.4. *MLAs*-based modeling of Micro-pore Attributes

K-fold Cross-validation (*CV*) [32] is a well-known method of determining the efficiency of the employed *MLAs* through random partitioning of the available data into *K*-sub groups with equal data distribution. The training of the *MLAs* is carried out utilizing data corresponding to (*K*-1) groups, following validation and performance evaluation using the left-out group. This *MLA*-based training and testing is conducted *K* times, that is 2, 5 or 10 times [34]. As a result, entire data set is utilized to evaluate the performance of the *MLA*-based modelling. This makes *K*-fold *CV* an unbiased, thorough and mostly accurate [30, 32, 33]. Results of *K*-fold *CV*, namely R^2 , *RMSE* and *AAPD* of the employed *MLAs*, are summarized in Fig. 10 – 12. Results indicate the *IBk* and *LWL* to perform the best and worst, respectively.

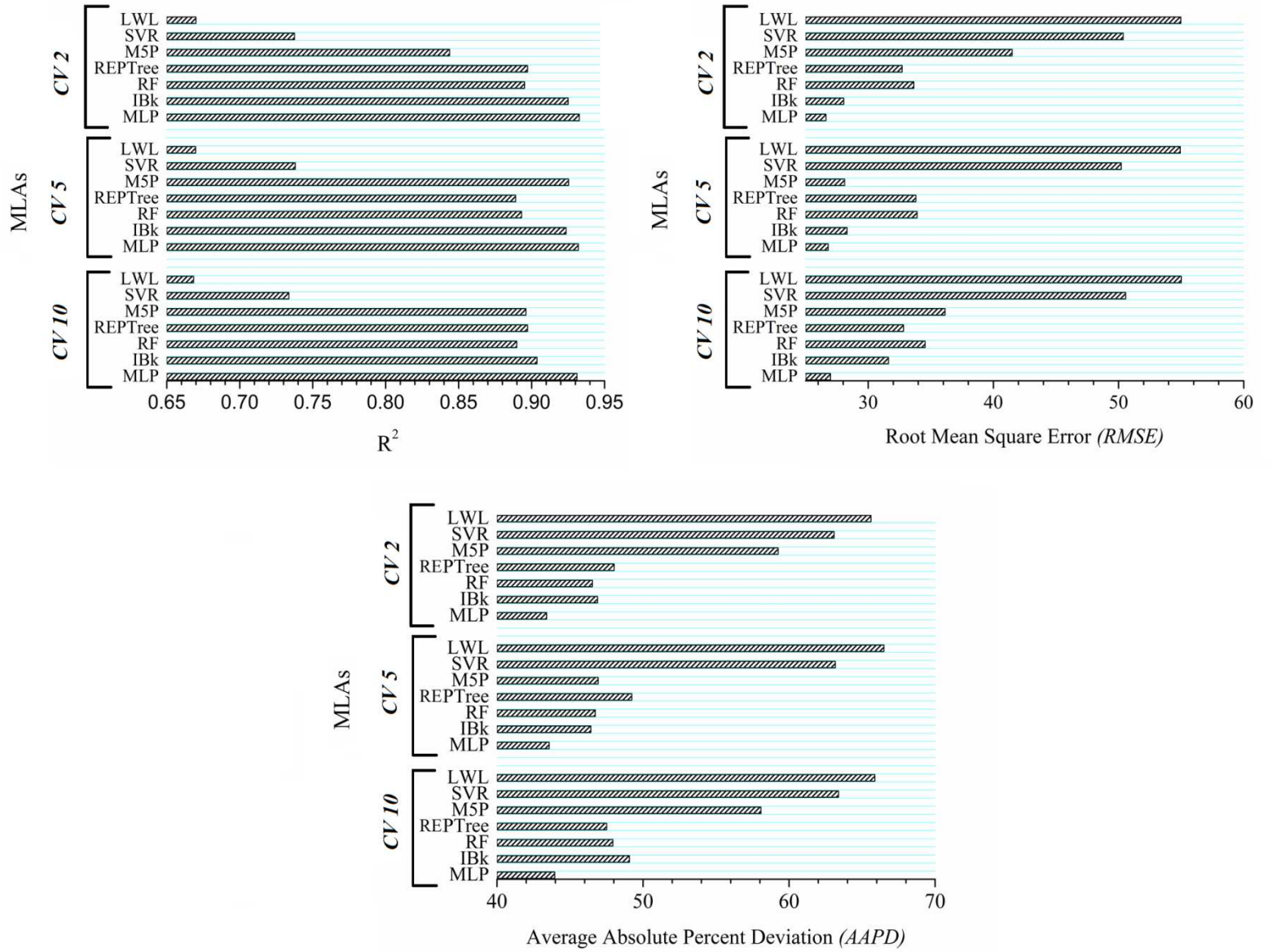
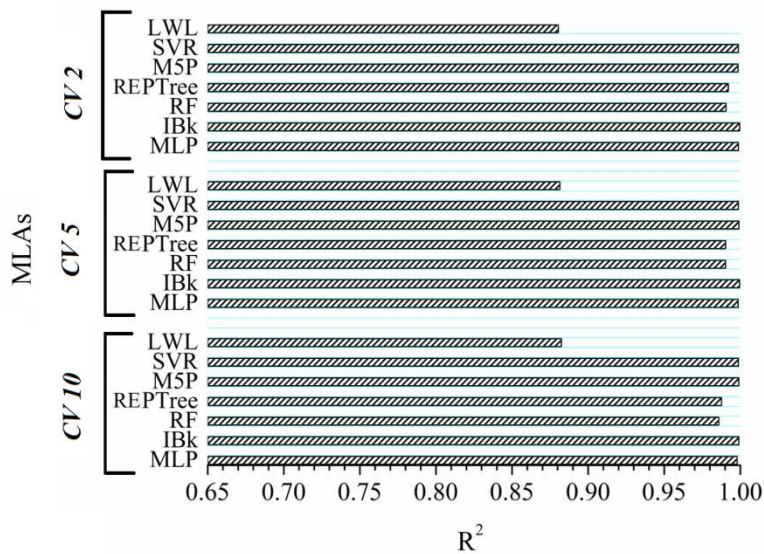
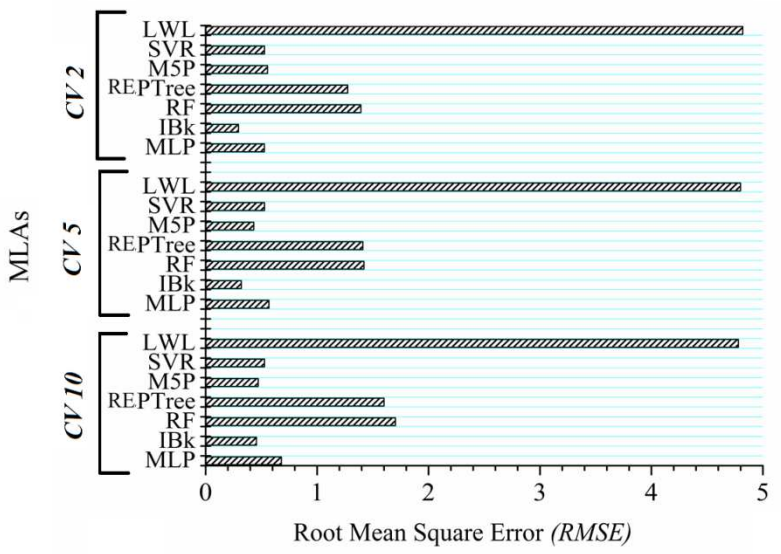


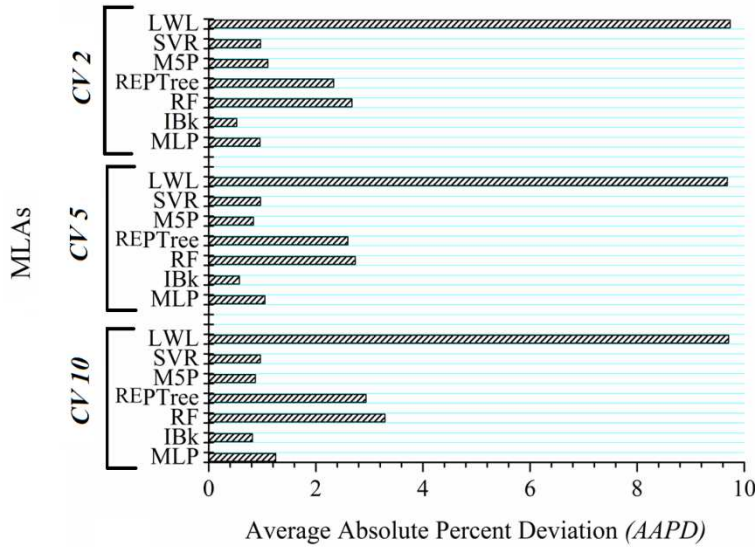
Fig. 10. Performance comparison of the employed models during the prediction of pore number (N_p) using
a) R^2 , b) $RMSE$, c) $AAPD$.



(a)



(b)



(c)

Fig. 11. Performance comparison of the employed models during the prediction of average pore diameter (D_p) using a) R^2 , b) RMSE, c) AAPD.

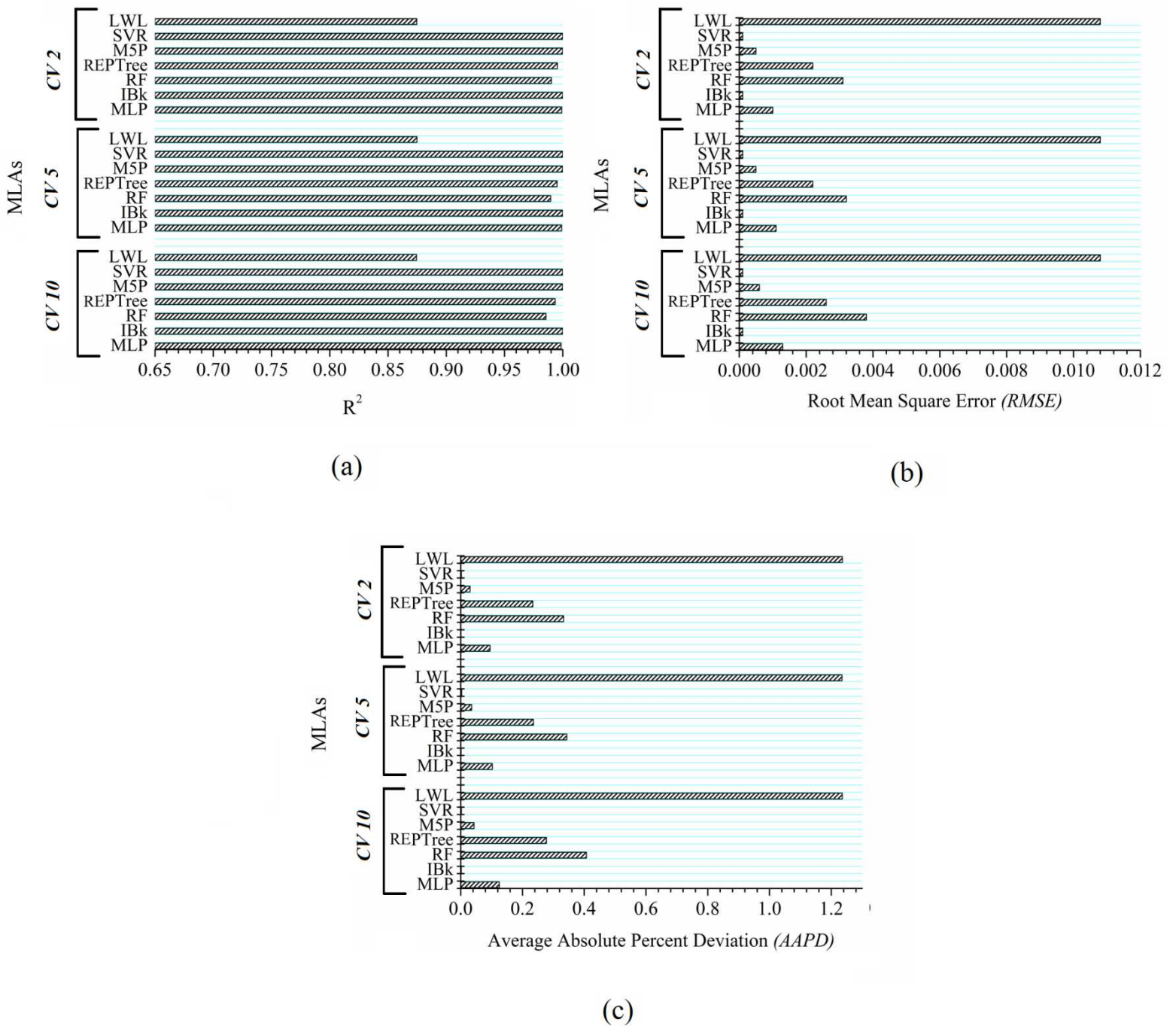


Fig 12. Performance comparison of the employed models during the prediction of average pore sphericity (S_{phry}) using a) R^2 , b) RMSE, c) AAPD.

All the employed models have successfully predicted the micro-porosity attributes with reasonable accuracy. *MLP* is observed to perform the best during the prediction of the number of pores. However, *IBk* has performed slightly better in predicting the average diameter and sphericity. As a result, *IBk* is found to perform the overall best, while *LWL* has performed relatively worse. The difference in the performances of *IBk* and *MLP* is found to be almost negligible. The non-parametric nature of handling data set might have led *IBk* to perform better. Similar better performance of *IBk* is also observed in the literature [62, 63]. Additionally, *MLP* also has performed well due to its robust neural network architecture. However, the poor performance of *LWL* may be attributed to its piece-wise problem simplification, which may have failed to tackle the non-linearity of the present problem [30, 57]. Schaal et al. [57] have stated that *LWL* is traditionally considered to perform inefficiently in high-dimensional spaces.

4.5. Performance evaluation of the MLAs through Statistical analysis

The performances of the different employed *MLAs* are compared through Friedman, Aligned Friedman and Quade statistical tests [64, 65], as provided in Tables 2.

Table 2. Performance-based ranking of *MLAs* employing Friedman, Aligned Friedman and Quade tests.

Algorithm	Friedman	Aligned Friedman	Quade
<i>IBk</i>	1.67	17.33	2.02
<i>MLP</i>	2.78	20.56	2.13
<i>SVR</i>	3.67	36.22	4.47
<i>M5P</i>	3.44	31.22	3.80
<i>RF</i>	4.89	32.89	4.22
<i>LWL</i>	7.00	56.33	7.00
<i>REPTree</i>	4.56	29.44	4.36
Statistics	33.67	7.76	7.22
p-value	7.80E-06	2.57E-01	1.57E-05

Table 2 suggests that *IBk* and *LWL* algorithms have performed the best and worst, respectively. Moreover, the differences in performance of most of the employed *MLAs* through statistical analyses are observed to be negligible. This shows that the employed *MLAs* are very competitive to one another in terms of quality of prediction.

4.6. Performance evaluation of the MLAs through Monte-Carlo reliability analysis

Monte Carlo technique utilizes random numbers to determine reliability of different systems [66]. This is done by calculating the probability of success ($p_{occurrence}$) for a pre-defined condition assumed to lie within the range of $\pm 5\%$ to $\pm 30\%$ in the present study. The reliability of the employed *MLAs* in predicting different micro-pore attributes are analyzed through a new data set of 10000 input data, generated utilizing random number generator. Eqs. (2-4) are then used to obtain regression equation predicted micro-pore attributes. The different *MLAs* are also utilized to obtain micro-pore attributes corresponding to the said 10000 input parameters. The different micro-pore attributes, predicted using the *MLAs* are grouped into success and failure conditions. That is, if the predicted value exceeds the domain, then it is considered as a failure. Else, it is considered to be successful. By following this rule, $p_{occurrence}$ is determined using Eq. (6),

$$p_{occurrence} = \frac{N_{success}}{N_{total}}, \quad (6)$$

where $N_{success}$ and N_{total} denote the successful and complete scenarios, respectively. $p_{occurrence}$ is determined in the pre-defined range, as shown in Fig. 13. The performance of *MLP*, *IBk* and *RF* are observed to be very close. On the other hand, *LWL* has performed the worst for the present problem. This observation is in line with the previous observations.

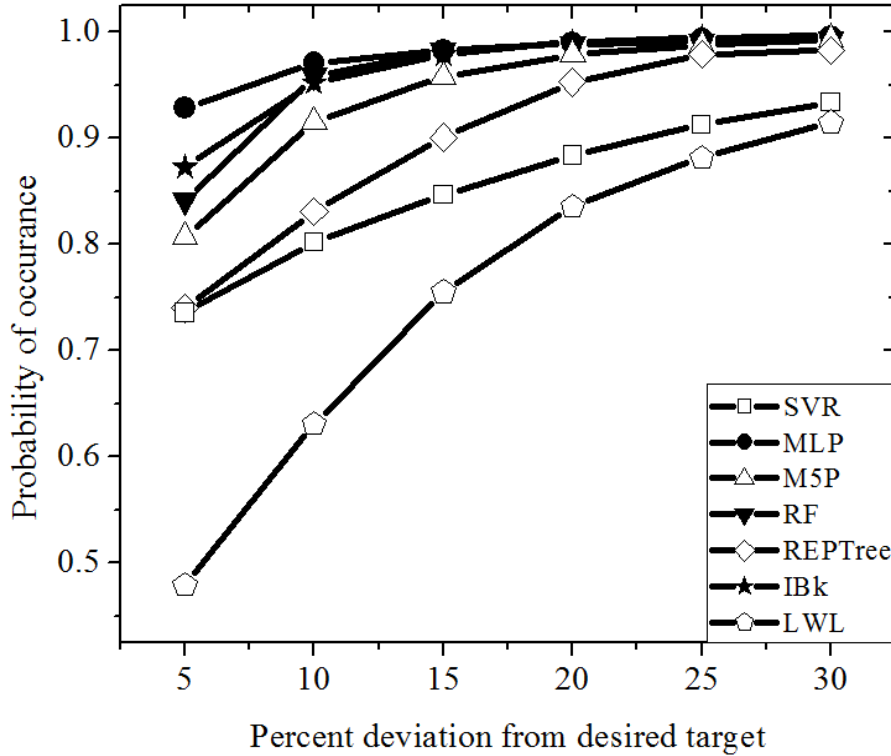


Fig. 13. Reliability of *MLAs* in predicting micro-pore attributes with the help of Monte-Carlo Reliability analysis.

Thus, the above stated *MLAs* having distinctly different backgrounds effectively have modeled the micro-porosity attributes in *EBW*. *MLP* from *ANN*-background and *IBk* from lazy-learner background are observed to perform well. On the other hand, the performances of *SVR* and *LWL* from the same *ANN* and lazy-learner backgrounds, respectively, are seen to be relatively less impressive.

5. Conclusion

An elaborate experimental study of micro-porosity during the *EBW* of AISI 304 Stainless Steel plates followed by an extended machine learning-based modeling is reported in the present study. The performances of these *MLAs* are also checked through statistical tests and Monte-Carlo reliability analysis. From the above study, the following conclusions are drawn:

1. The number and size of pores in the weld zone are found to increase initially and then, decrease with an increase in the heat input.

2. The average pore sphericity and pore diameter showed an inverse relation, which is in accordance with the literature.
3. Hydrogen and nitrogen gases are identified inside the pores. The smaller pores are formed by nucleation and growth during solidification. The bigger and irregular pores are most likely to be formed due to shrinkage. The smaller pores are found to be more spherical than the bigger ones.
4. Large melt area with the slower cooling rate is observed to increase the chance of gases' escape from weld zone.
5. Machine learning algorithms-predicted weld-micro-porosity attributes have closely matched with the experimental ones, and could be applied in industrial applications.
6. Reliable and robust modeling of weld micro-porosity is possible due to the use of multiple techniques from the distinctly different backgrounds.
7. *MLP* and *IBk* are found to perform well, while the performances of *SVR* and *LWL* are observed to be inadequate.
8. Results obtained through statistical tests and Monte-Carlo reliability analysis endorse the superiority in performance of *IBk* and *MLP* over the rest.

Ethical Approval: Yes

Consent to Participate: Yes

Consent to Publish: Yes

Authors Contributions:

Debasish Das: Experiment, Data Collection, Machine learning-based Modeling, Paper Writing

Soumitra Dinda: Experiment, Data collection; Paper Writing

Amit Kumar Das: Modeling, Paper Writing

Dilip Kumar Pratihar: Supervision, Reviewing and Editing

Gour Gopal Roy: Supervision, Reviewing and Editing

Funding: First three authors, namely Debasish Das, Soumitra Dinda, Amit Kumar Das received MHRD funding as their fellowships to carry out this research.

Competing Interests: There is no conflict of interests with others.

Availability of Data and Materials: The data and materials are available with the authors, which will be supplied to others on request.

References

1. Feng S, Zhou H, Dong H (2019) Using deep neural network with small dataset to predict material defects. *Mater Des* 162:300–310. <https://doi.org/10.1016/j.matdes.2018.11.060>
2. Mathew J, Griffin J, Alamaniotis M, et al (2018) Prediction of welding residual stresses using machine learning: Comparison between neural networks and neuro-fuzzy systems. *Appl Soft Comput J* 70:131–146. <https://doi.org/10.1016/j.asoc.2018.05.017>
3. Das D, Pal AR, Das AK, et al (2020) Nature-Inspired Optimization Algorithm-Tuned Feed-Forward and Recurrent Neural Networks Using CFD-Based Phenomenological Model-Generated Data to Model the EBW Process. *Arab J Sci Eng* 45:2779–2797. <https://doi.org/10.1007/s13369-019-04142-9>
4. Das D, Pratihar DK, Roy GG, Pal AR (2018) Phenomenological model-based study on electron beam welding process, and input-output modeling using neural networks trained by back-propagation algorithm, genetic algorithms, particle swarm optimization algorithm and bat algorithm. *Appl Intell* 48:2698–2718. <https://doi.org/10.1007/s10489-017-1101-2>
5. Das D, Pratihar DK, Roy GG (2018) Cooling rate predictions and its correlation with grain characteristics during electron beam welding of stainless steel. *Int J Adv Manuf Technol* 97:2241–2254. <https://doi.org/10.1007/s00170-018-2095-6>
6. Vilar R, Zapata J, Ruiz R (2009) An automatic system of classification of weld defects in radiographic images. *NDT E Int* 42:467–476. <https://doi.org/10.1016/j.ndteint.2009.02.004>
7. Hou W, Wei Y, Jin Y, Zhu C (2019) Deep features based on a DCNN model for classifying imbalanced weld flaw types. *Measurement* 131:482–489. <https://doi.org/10.1016/j.measurement.2018.09.011>
8. Lu F, Li X, Li Z, et al (2015) Formation and influence mechanism of keyhole-induced porosity in deep-penetration laser welding based on 3D transient modeling. *Int J Heat Mass Transf* 90:1143–1152. <https://doi.org/10.1016/j.ijheatmasstransfer.2015.07.041>
9. Sun J, Nie P, Lu F, et al (2017) The characteristics and reduction of porosity in high-power laser welds of thick AISI 304 plate. *Int J Adv Manuf Technol* 93:3517–3530.

<https://doi.org/10.1007/s00170-017-0734-y>

10. Wang J, Wang GZ, Wang CM (2015) Mechanisms of the porosity formation during the fiber laser lap welding of aluminium alloy. *Metalurgija* 54:683–686
11. Dinda SK, Warnett JM, Williams MA, et al (2016) 3D imaging and quantification of porosity in electron beam welded dissimilar steel to Fe-Al alloy joints by X-ray tomography. *Mater Des* 96:224–231. <https://doi.org/10.1016/j.matdes.2016.02.010>
12. Elmer JW, Vaja J, Carlton HD, Pong R (2015) The Effect of Ar and N₂ Shielding Gas on Laser Weld Porosity in Steel, Stainless Steels, and Nickel. *Weld J* 94:313–325
13. Lisiecki A (2016) Effect of heat input during disk laser bead-on-plate welding of thermomechanically rolled steel on penetration characteristics and porosity formation in the weld metal. *Arch Metall Mater* 61:93–102. <https://doi.org/10.1515/amm-2016-0019>
14. Blecher J, Palmer T, Debroy T (2015) Mitigation of Root Defect in Laser and Hybrid Laser-Arc Welding. *Weld Res* 94:73-s-82-s
15. Bandi B, Dinda SK, Kar J, et al (2018) Effect of weld parameters on porosity formation in electron beam welded Zircaloy-4 joints: X-ray tomography study. *Vacuum* 158:172–179. <https://doi.org/10.1016/j.vacuum.2018.09.060>
16. Dinda SK, kar J, Jana S, et al (2019) Effect of beam oscillation on porosity and intermetallics of electron beam welded DP600-steel to Al 5754-alloy. *J Mater Process Technol* 265:191–200. <https://doi.org/10.1016/j.jmatprotec.2018.10.026>
17. Ramanujam T, Devai HP, Gopi M, et al (2018) Porosity studies on electron beam welding of copper alloys. *Int J Mech Eng Technol* 9:586–593
18. Alshaer AW, Li L, Mistry A (2014) Understanding the Effect of Heat Input and Sheet Gap on Porosity Formation in Fillet Edge and Flange Couch Laser Welding of AC-170PX Aluminum Alloy for Automotive Component Manufacture. *J Manuf Sci Eng* 137:021011. <https://doi.org/10.1115/1.4028900>
19. Zhan X, Qi C, Gao Z, et al (2019) The influence of heat input on microstructure and porosity during laser cladding of Invar alloy. *Opt Laser Technol* 113:453–461. <https://doi.org/10.1016/j.optlastec.2019.01.015>
20. Xie MX, Li YX, Shang XT, et al (2019) Effect of heat input on porosity defects in a fiber laser welded socket-joint made of powder metallurgy molybdenum alloy. *Materials (Basel)* 12:. <https://doi.org/10.3390/ma12091433>
21. Jha MN, Pratihar DK, Dey V, et al (2011) Study on electron beam butt welding of austenitic stainless steel 304 plates and its input-output modelling using neural networks. *Proc Inst Mech Eng Part B-Journal Eng Manuf* 225:2051–2070. <https://doi.org/10.1177/0954405411404856>

22. Petkovi D (2017) Prediction of laser welding quality by computational intelligence approaches. *Optik* (Stuttg) 140:597–600. <https://doi.org/10.1016/j.ijleo.2017.04.088>
23. Liang R, Yu R, Luo Y, Zhang YM (2019) Machine learning of weld joint penetration from weld pool surface using support vector regression. *J Manuf Process* 41:23–28. <https://doi.org/10.1016/j.jmapro.2019.01.039>
24. Boersch I, Füssel U, Gresch C, et al (2018) Data mining in resistance spot welding: A non-destructive method to predict the welding spot diameter by monitoring process parameters. *Int J Adv Manuf Technol* 99:1085–1099. <https://doi.org/10.1007/s00170-016-9847-y>
25. Ghanty P, Paul S, Mukherjee DP, et al (2007) Modelling weld bead geometry using neural networks for GTAW of austenitic stainless steel. *Sci Technol Weld Join* 12:649–658. <https://doi.org/10.1179/174329307X238399>
26. Munir N, Kim H, Park J, et al (2018) Convolutional neural network for ultrasonic weldment flaw classification in noisy conditions. *Ultrasonics*. <https://doi.org/10.1016/j.ultras.2018.12.001>
27. Wang G, Liao TW (2002) Automatic identification of different types of welding defects in radiographic images. *Ndt E Int* 35:519–528
28. Liao TW, Triantaphyllou E, Chang PC (2003) Detection of Welding Flaws With MLP Neural Network and Case Based Reasoning. *Intell Autom Soft Comput* 4:259–267. <https://doi.org/10.1080/10798587.2000.10642858>
29. Das D, Jaypuria S, Pratihar DK, Roy GG (2021) Weld optimisation (Review). *Sci Technol Weld Join*. <https://doi.org/https://doi.org/10.1080/13621718.2021.1872856>
30. Namlı E, Erdal H, Erdal H. I (2019) Artificial Intelligence-Based Prediction Models for Energy Performance of Residential Buildings. In: Balkaya N, Guneysu S (eds) *Recycling and Reuse Approaches for Better Sustainability*. Springer International Publishing, Cham, Switzerland, p 304
31. Özçift A (2014) Forward stage-wise ensemble regression algorithm to improve base regressors prediction ability: An empirical study. *Expert Syst* 31:1–8. <https://doi.org/10.1111/j.1468-0394.2012.00643.x>
32. Maji K (2014) Analysis and Synthesis of Sheet Metal Forming by Laser Heating Using Finite Element Method and Soft Computing (Doctoral dissertation, IIT Kharagpur). <http://www.idr.iitkgp.ac.in/xmlui/handle/123456789/3780>
33. Haykin S (2005) *Neural Networks - A Comprehensive Foundation*. 823
34. Das D, Das AK, Pratihar DK, Roy GG (2020) Prediction of Residual Stress in Electron Beam Welding of Stainless Steel from Process Parameters and Natural Frequency of Vibrations Using Machine-Learning Algorithms. *Proc Inst Mech Eng Part C J Mech Eng Sci* 0954406220950343. <https://doi.org/10.1177/0954406220950343>

35. Xia X, Wu J, Liu Z, et al (2019) Study of microstructure difference properties of electron beam welds with beam oscillation of 50 mm 316L in CFETR. *Fusion Eng Des* 138:339–346. <https://doi.org/10.1016/j.fusengdes.2018.12.011>
36. Fu P, Mao Z, Zuo C, et al (2014) Microstructures and fatigue properties of electron beam welds with beam oscillation for heavy section TC4-DT alloy. *Chinese J Aeronaut* 27:1015–1021. <https://doi.org/10.1016/j.cja.2014.03.020>
37. Das D, Pratihar DK, Roy GG (2020) Establishing a Correlation Between Residual Stress and Natural Frequency of Vibration for Electron Beam Butt Weld of AISI 304 Stainless Steel. *Arab J Sci Eng* 45:5769–5781. <https://doi.org/10.1007/s13369-020-04560-0>
38. Das D, Pratihar DK, Roy GG. (2016) Electron Beam Melting of Steel Plates: Temperature Measurement Using Thermocouples and Prediction Through Finite Element Analysis. In: Mandal DK, Syan CS (eds) CAD/CAM, Robotics and Factories of the Future. Springer, New Delhi, pp 579–588
39. Chen YY, Duval T, Hung UD, et al (2005) Microstructure and electrochemical properties of high entropy alloys-a comparison with type-304 stainless steel. *Corros Sci* 47:2257–2279. <https://doi.org/10.1016/j.corsci.2004.11.008>
40. Kumar S, Shahi AS (2011) Effect of heat input on the microstructure and mechanical properties of gas tungsten arc welded AISI 304 stainless steel joints. *Mater Des* 32:3617–3623. <https://doi.org/10.1016/j.matdes.2011.02.017>
41. Das D (2020) Predictive Tools for Bead-Geometry, Cooling Rate, Micro-Porosity, Natural Frequency of Vibration and Residual Stress in Electron Beam Welded Stainless Steel Plates (Doctoral dissertation, IIT Kharagpur). Indian Institute of Technology Kharagpur, India
42. James TM, Rupp S, Telle HH (2015) Trace gas and dynamic process monitoring by Raman spectroscopy in metal-coated hollow glass fibres. *Anal Methods* 7:2568–2576. <https://doi.org/10.1039/c4ay02597k>
43. Buric MP (2011) Gas Phase Raman Spectroscopy using Hollow Waveguides (Doctoral dissertation, Swanson School of Engineering), University of Pittsburgh, United States
44. Leitch AWR, Alex V, Weber J (1998) Raman Spectroscopy of Hydrogen Molecules in Crystalline Silicon. *Phys Rev Lett* 81:421
45. Das D, Pratihar DK, Roy GG (2020) Effects of space charge on weld geometry and cooling rate during electron beam welding of stainless steel. *Optik (Stuttg)* 206:163722. <https://doi.org/10.1016/j.ijleo.2019.163722>
46. Graczyk M, Lasota T, Trawinski B (2009) Comparative analysis of premises valuation models using KEEL, RapidMiner, and WEKA. In: International conference on computational collective

- intelligence. Springer Berlin Heidelberg, pp 800–812
47. Hsieh CH, Lu RH, Lee NH, et al (2011) Novel solutions for an old disease: Diagnosis of acute appendicitis with random forest, support vector machines, and artificial neural networks. *Surgery* 149:87–93. <https://doi.org/10.1016/j.surg.2010.03.023>
48. Amrehn M, Mualla F, Angelopoulou E, et al (2018) The Random Forest Classifier in WEKA: Discussion and New Developments for Imbalanced Data. *arXiv Prepr arXiv181208102*
49. Zahara SI, Ilyas M, Zia T (2013) A study of comparative analysis of regression algorithms for reusability evaluation of object oriented based software components. *ICOSST 2013 - 2013 Int Conf Open Source Syst Technol Proc* 75–80. <https://doi.org/10.1109/ICOSST.2013.6720609>
50. Alam I, Farid DM, Rossetti RJF (2019) The Prediction of Traffic Flow with Regression Analysis. In: *Emerging Technologies in Data Mining and Information Security*. Springer Singapore, pp 661–671
51. Martín Ó, Pereda M, Santos JI, Galán JM (2014) Assessment of resistance spot welding quality based on ultrasonic testing and tree-based techniques. *J Mater Process Technol* 214:2478–2487. <https://doi.org/10.1016/j.jmatprotec.2014.05.021>
52. Xing B, Xiao Y, Qin QH, Cui H (2018) Quality assessment of resistance spot welding process based on dynamic resistance signal and random forest based. *Int J Adv Manuf Technol* 94:327–339. <https://doi.org/10.1007/s00170-017-0889-6>
53. Göndör M, Bresfelean VP (2012) REPTree and M5P for measuring fiscal policy influences on the Romanian capital market during 2003-2010. *Int J Math Comput Simul* 6:378–386
54. Vapnik V (2013) *The nature of statistical learning theory*. Springer-Verlag New York Inc
55. Chen J, Wang T, Gao X, Li W (2018) Real-time monitoring of high-power disk laser welding based on support vector machine. *Comput Ind* 94:75–81. <https://doi.org/10.1016/j.compind.2017.10.003>
56. Zhan C, Gan A, Hadi M (2011) Prediction of lane clearance time of freeway incidents using the M5P tree algorithm. *IEEE Trans Intell Transp Syst* 12:1549–1557. <https://doi.org/10.1109/TITS.2011.2161634>
57. Schaal S, Atkeson CG, Vijayakumar S (2002) Real-time robot learning with locally weighted statistical learning. 288–293. <https://doi.org/10.1109/robot.2000.844072>
58. Katayama S, Kawahito Y, Mizutani M (2007) Collaboration of physical and metallurgical viewpoints for understanding and process development of laser welding. In: *26th International Congress on Applications of Lasers & Electro-Optics (ICALEO)*. Orlando, LIA, pp 360–369
59. Dinda SK, Srirangam P, Roy GG (2019) Effects of Beam Oscillation on Porosity and Intermetallic Compounds Formation of Electron Beam Welded DP600 Steel to Al-5754 Alloy Joints. In: *148th Annual Meeting & Exhibition Supplemental Proceedings, The Minerals, Metals & Materials Series*

(TMS). Springer International Publishing, pp 239–249

60. Huang JL, Warnken N, Gebelin J, et al (2012) On the mechanism of porosity formation during welding of titanium alloys. *Acta Mater* 60:3215–3225. <https://doi.org/10.1016/j.actamat.2012.02.035>
61. Tammas-williams S, Zhao H, Léonard F, et al (2015) XCT analysis of the influence of melt strategies on defect population in Ti – 6Al – 4V components manufactured by Selective Electron Beam Melting. *Mater Charact* 102:47–61. <https://doi.org/10.1016/j.matchar.2015.02.008>
62. Novakovic JD, Veljovic A, Ilic SS, Papic M (2016) Experimental study of using the k-nearest neighbour classifier experimental study of using the k-nearest neighbour classifier with filter methods. In: Computer Science and Technology. Varna, Bulgaria, pp 90–99
63. Pan R, Yang T, Cao J, et al (2015) Missing data imputation by K nearest neighbours based on grey relational structure and mutual information. *Appl Intell* 43:614–632. <https://doi.org/10.1007/s10489-015-0666-x>
64. Derrac J, García S, Molina D, Herrera F (2011) A practical tutorial on the use of nonparametric statistical tests as a methodology for comparing evolutionary and swarm intelligence algorithms. *Swarm Evol Comput* 1:3–18. <https://doi.org/10.1016/j.swevo.2011.02.002>
65. Chakri A, Khelif R, Benouaret M, Yang XS (2017) New directional bat algorithm for continuous optimization problems. *Expert Syst Appl* 69:159–175. <https://doi.org/10.1016/j.eswa.2016.10.050>
66. Takeshi M (2013) The Monte Carlo Simulation Method for System Reliability and Risk Analysis. *Nucl Saf Simul* 4:44–52. <https://doi.org/10.1007/978-1-4471-4588-2>